ChemPubSoc Europe

DOI: 10.1002/cctc.201802019

CHEMCATCHEM Full Papers

Intercalating MnO_2 Nanosheets With Transition Metal Cations to Enhance Oxygen Evolution

Yue Yang,[a, b] Xingsong Su,[b] Lei Zhang,[b] Peter Kerns,[b] Laura Achola,[b] Veronica Hayes,[b] Rebecca Quardokus,[b] Steven L. Suib,*[b, c, d] and Jie He*[b, d]

The catalytic activity of MnO_2 nanosheets towards oxygen evolution depends highly on their interlayer environment. We present a systematic investigation on fine-tuning of the interlayer environment of MnO_2 nanosheets by intercalation through a facile cation exchange with inexpensive first-row transition metal cations, including Ni^{2+}, Co^{2+}, Cu^{2+}, Zn^{2+}, and Fe^{3+} ions. Among them, the Ni-intercalated MnO_2 nanosheets show remarkably enhanced OER activity and long-term stability, compared to pristine MnO_2 nanosheets. The overpotential of 330 mV at a current density of 10 mA cm^{-2} is observed for the Ni-intercalated MnO_2 nanosheets. The ehancement mechanism of OER is studied by comparing physiochemical properties, such as the oxidation state of Mn, the interlayer distance, the increase in the disorder/twisting of MnO_6 octahedra, and the interlayer cooperative binding of water molecules. The Ni intercalation, different from other metal cations, strengthens the Mn–O bond perpendicularly to the layer chains to facilitate the interlayer catalysis possibly between two Mn sites, and thus promotes the efficiency of oxygen evolution.

Introduction

Efficiently converting sustainable and renewable energy (*e.g.*, solar energy) to chemical energy is desirable in the hope of eliminating the use of fossil fuels and transforming our energy supply system.[1] Water splitting to H_2 and O_2 has been long recognized as a promising strategy for the mass production of the alternative clean energy, *e.g.*, H_2, driven by solar energy or electricity from renewable resources.[2] However, the sluggish kinetics and large overpotential of the $4e^-$ involved oxygen evolution reaction (OER) is a bottleneck towards overall water splitting.[3] Precious metal oxides *e.g.*, RuO_2 and IrO_2, among the best electrocatalysts for OERs, still show a high overpotential (η, >300 mV) to drive the oxidation of water.[4]

Developing more active catalysts in order to lower the energy barrier for OERs has attracted considerable attention over decades. Taking inspiration from nature where the manganese-containing cluster (Mn_4O_8Ca) in photosystem II shows extremely high activity with a turnover frequency of 100 s^{-1},[5] substantial efforts have been devoted to studying inexpensive manganese-containing catalysts for OERs instead of high-cost precious metal or metal oxides.[6] In particular, Mn oxides/hydroxides with different oxidation states such as MnO,[7] MnO_2,[8] Mn_2O_3,[9] MnOOH,[10] and complex oxides like Co-, Cu-, Ca-doped MnO_2 [3,11] have been intensively studied in OER catalysis. Among many polymorphs of MnO_2, layered Mn oxide (δ-MnO_2, or birnessite) consisting of two-dimensional (2D)-layered structures with edge-sharing MnO_6 octahedra is a potential candidate for OERs. However, the catalytic activity of bulk δ-MnO_2 is very low among various polymorphs of MnO_2.[5d,12] The catalytic activity of δ-MnO_2 for the OER is sensitive to the interlayer environment of layered materials. Therefore, the possibility of controlling the interlayer properties by readily exchanging the guest cations with a range of metal cations like K^+, Na^+, Mg^{2+}, Zn^{2+}, Ni^{2+}, and Co^{2+} ions,[13] possibly can promote the tunable electrochemical activity for OERs. Kang *et al.*[14] and Xiong *et al.*[15] demonstrated that the expanded interlayer spacing of MnO_2 nanosheets by intercalating large cations contributed to the increased catalytic activity towards OER and the electrochemical energy storage capacity. Recent studies from Strongin's group showed that the confinement of Cu^{2+}, Co^{2+}, and Ni^{2+} into the interlayer of birnessite led to the enhancement in the activity towards OER where Co^{2+}/birnessite could achieve 10 mA cm^{-2} at a low overpotential of 360 mV.[16]

MnO_2 nanosheets with single- or few-layers are closely related to bulk δ-MnO_2. The ultrathin nanosheets with atomic thickness possess highly accessible surfaces within the interlayers and maximum exposed active sites, thus facilitating

[a] Y. Yang
Department of Chemical Engineering
Nanjing University of Science and Technology
Nanjing 210094 (China)
[b] Y. Yang, Dr. X. Su, Dr. L. Zhang, P. Kerns, L. Achola, V. Hayes, Prof. Dr. R. Quardokus, Prof. Dr. S. L. Suib, Prof. Dr. J. He
Department of Chemistry
University of Connecticut
Storrs, CT 06269 (USA)
E-mail: steven.suib@uconn.edu
jie.he@uconn.edu
[c] Prof. Dr. S. L. Suib, Prof. Dr. J. He
Institute of Materials Science
University of Connecticut
Storrs, CT 06269 (USA)
[d] Prof. Dr. S. L. Suib
Department of Chemical & Biomolecular Engineering
University of Connecticut
Storrs, CT 06269 (USA)

Supporting information for this article is available on the WWW under https://doi.org/10.1002/cctc.201802019

This publication is part of the Young Researchers Series. More information regarding these excellent researchers can be found on the ChemCatChem homepage.

Table 1. Nitrogen adsorption analysis and atomic ratio of intercalated MnO_2 characterized by XRF, XPS and SEM-EDX mapping.

Sample	Feeding molar ratio of Mn:M	Exchange time [h]	K/Mn [%] XRF	M/Mn [%] XRF	M/Mn [%] XPS	M/Mn [%] EDX	BET surface area [$m^2 g^{-1}$]
MnO_2	/	/	8.4	/	/	/	114
Ni–MnO_2	1:3	12	0.6	18.3	12.7	11.1	280
Co–MnO_2	1:3	12	1.0	25.1	16.6	15.5	165
Cu–MnO_2	1:3	12	0.4	28.8	10.1	21.4	290
Zn–MnO_2	1:3	12	0.8	21.3	13.9	15.7	209
Fe–MnO_2	1:3	12	0.5	71.4	61.7	55.5	315
Ni-doped MnO_2	1:0.1	1	/	/	/	12.3	/
Ni-doped MnO_2/K^+	1:0.1	12	/	/	/	11.4	/

interfacial charge transfer and efficient catalysis.[17] This enables the MnO_2 nanosheets to gain the extraordinarily improved catalytic activity and high specific capacitance as a pseudocapacitor material compared to their bulk counterparts. Zhao *et al.* reported that ultrathin two-monolayer MnO_2 nanosheet arrays (1.4 nm) grown on Ni foam exhibited efficient water splitting with a low overpotential of 320 mV at 10 mA cm^{-2} for OER.[18] Recently, single-layer MnO_2 nanosheets prepared and ordered by sodium dodecyl sulfate (SDS) without any exfoliation agents were developed by Liu *et al.*[19] The superior specific capacitance of 868 F g^{-1} at current density of 3 A g^{-1} and excellent cycling stability (91% retained after 10 000 charge/discharge cycles) was achieved with single-layer MnO_2 nanosheets. Various ultrathin transition metal oxides and hydroxides/oxyhydroxides nanosheets have also drawn tremendous attention other than Mn-containing materials, for instance γ-CoOOH nanosheets,[20] amorphous cobalt-iron hydroxide nanosheets,[21] layered double hydroxides,[22] α-$Ni(OH)_2$, and NiO nanosheets,[23] *etc.* Given the fascinating electronic structure and the largely accessible surface sites, ultrathin nanosheets stand out as one of the most promising candidates as anode materials for OERs.

Herein, we report the intercalation of transition metal cations including Ni^{2+}, Co^{2+}, Cu^{2+}, Zn^{2+}, and Fe^{3+} ions into the interlayer region of MnO_2 nanosheets via a facile cation exchange approach. A series of characterization techniques such as electron spectroscopy, X-ray diffraction, X-ray photoelectron spectroscopy, Raman spectra, and Fourier-transform infrared spectra are used to confirm the successful intercalation of metal cations and investigate how the intercalation varies the physiochemical properties of MnO_2 nanosheets. For Ni-intercalated MnO_2 nanosheets, the evidently enhanced OER activity with a significantly lower overpotential of 330 mV at a current density of 10 mA cm^{-2} and a high TOF of 0.0356 s^{-1} is achieved, compared to that of pristine MnO_2 nanosheets (η = 581 mV). Interestingly, Ni-intercalated MnO_2 nanosheets interlayerly show better activity compared to Ni-doped MnO_2 nanosheets. Multiple factors resulting in the improvement of OER activity were studied in detail, including the oxidation state of Mn, structural disorder caused by metal cations, electron transfer and interlayer cooperative catalysis. The Ni-intercalated MnO_2 nanosheets with dynamically mobile Ni ions can improve the cooperative binding with water through two Mn sites, which is believed to be of great importance for the catalytic activity of MnO_2 nanosheets.

Results

Synthesis and Characterization

The layered MnO_2 nanosheets were synthesized through the reduction of $KMnO_4$ in the presence of SDS.[19] As-prepared MnO_2 nanosheets are ultrathin, flaky with an average lateral dimension of 1 ~ 5 μm. The typical 2D nanostructures of nanosheets were examined using scanning electron microscopy (SEM) and transmission electron microscopy (TEM) (Figure 1a, c). As determined from the warped edges of the nanosheets, the individual nanosheet exhibits a thickness of ~1.4 nm (see the inset of Figure 1b), corresponding to 2–3 layers of nanosheets. The edge height of nanosheets measured by atomic force microscopy (AFM) is around 8 nm (Figure 1j, k). This suggests that MnO_2 nanosheets are flexible and warp when drying onto the substrate; and the edge of the MnO_2 nanosheets can fold/stack with each other as seen in TEM. The metal-intercalated nanosheets were obtained by a simple cation exchange at room temperature due to high capacity of guest cations accommodated in the interlayer region, using metal nitrate salts of Ni^{2+}, Co^{2+}, Cu^{2+}, Zn^{2+}, and Fe^{3+}. Those intercalated materials are denoted as M–MnO_2 (M = Ni, Co, Cu, Zn, Fe) nanosheets. The typical lamellar morphologies for layered pristine MnO_2 nanosheets were retained after the intercalation of Ni^{2+}, Co^{2+}, Cu^{2+}, and Zn^{2+}, as shown in Figure 1c-g. In addition, the thickness of the nanosheets after intercalation did not undergo any obvious change. Single nanosheets still remained with thicknesses of ~1.2 nm (see the inset of Figure 1d). Similar re-stacking of Ni-MnO_2 was also observed from AFM analysis in Figure 1l, m.

SEM energy dispersive X-ray spectroscopy (EDX) was used to confirm the intercalation. Figure 1i shows the SEM-EDX mapping of Ni–MnO_2. The intercalated MnO_2 displays a uniform distribution of Mn, O, and Ni elements, indicating the successful exchange between Ni^{2+} and K^+ (Figure S1). Meanwhile, the atomic concentrations of intercalated metal cations were co-determined by SEM-EDX mapping, XRF, and are listed in Table 1. The contents of the exchanged metal cations were all around 20–30 at%, as determined by XRF, except highly doped Fe (71.4 at%), showing the high accommodation capacity of MnO_2 nanosheets. The resultant proportion of the intercalating transition metal cations are usually related to the intrinsic properties of the cations, like radius, valence, charges, etc. Interestingly, the least exchange amount, 18.3 at%, was ob-

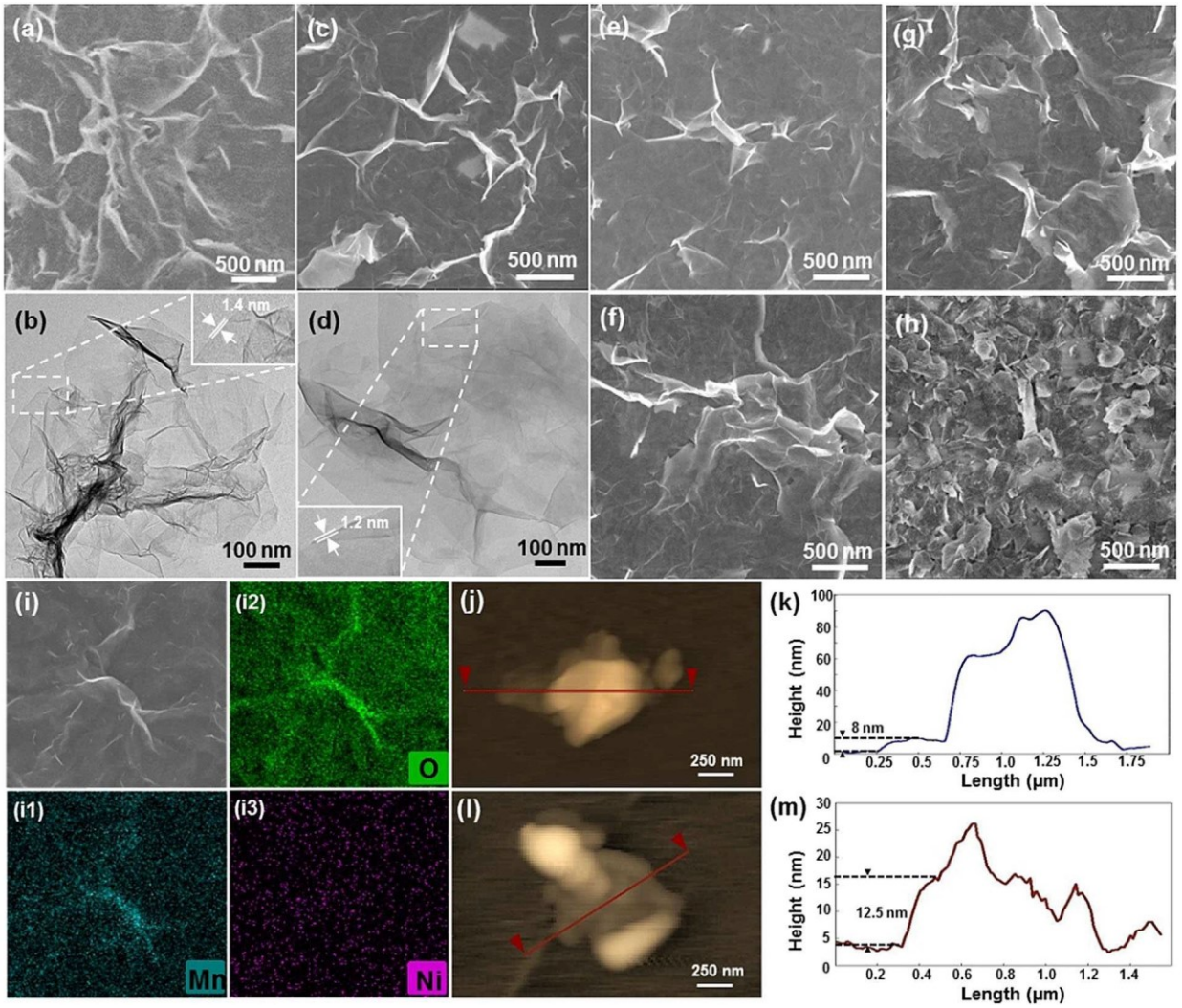

Figure 1. (a, c) SEM and (b, d) TEM images of pristine MnO_2 (a, b) and Ni–MnO_2 (c, d) nanosheets. The insets in (b, d) show the respective thickness of pristine and Ni intercalated MnO_2 nanosheets. (e-h) Respective SEM images of Co–MnO_2, Cu–MnO_2, Zn–MnO_2, and Fe–MnO_2 nanosheets. (i) SEM-EDX elemental mappings for Ni-MnO_2: Mn, O, and Ni are given in (i1–i3), respectively. (j–m) AFM images and corresponding height profiles of pristine MnO_2 (j, k) and Ni–MnO_2 nanosheets (l, m), respectively.

tained after Ni^{2+} (0.69 Å) intercalation as determined by XRF analysis. As followed, 21.3 at%, 25.1 at%, and 28.8 at% was intercalated as Zn^{2+} (0.74 Å), Co^{2+} (0.74 Å), and Cu^{2+} (0.73 Å) cations were fed. Due to the higher valence and much smaller radius (0.63 Å), Fe^{3+} resided in the interlayer region in the largest proportion (71.4 at%). The substitution of K^+ with metal ions was also indicated by the evident decrease of K^+ concentration from 8.4 at% (K/Mn) to below 1.0 at% and simultaneous increase of the corresponding metal cation concentration, as summarized in Table 1.

The Brunauer-Emmett-Teller (BET) surface areas calculated by N_2 adsorption-desorption isotherms are summarized in Table 1 and Figure S2. In comparison to pristine MnO_2 (114 $m^2 g^{-1}$), intercalated M–MnO_2 exhibited larger surface areas (specially, 280 $m^2 g^{-1}$ for Ni-MnO_2, 165 $m^2 g^{-1}$ for Co–MnO_2, 290 $m^2 g^{-1}$ for Cu–MnO_2, 209 $m^2 g^{-1}$ for Zn-MnO_2, 315 $m^2 g^{-1}$ for Fe–MnO_2). The increase in surface area after intercalation is indicative of the slightly larger accessible active surface that potentially improves electrocatalytic performance as discussed below.

The characteristic crystal structure of pristine MnO_2 nanosheets (JCPDS No. 80-1098, OL-1, Octahedral layered birnessite) was also confirmed by X-ray diffraction (XRD) in Figure 2a.[24] The crystal destruction, to some extent, was observed for intercalated M–MnO_2 nanosheets, since the broadening of the diffraction peak (001) was seen in XRD patterns. The intercalation of metal cations including Ni^{2+}, Co^{2+}, Cu^{2+}, and Zn^{2+} led to a slight shift of (001) and (002) towards a higher 2θ relative to the pristine MnO_2, indicating the contraction of the interlayer spacing. [6a–c,25] The *d*-spacings presented in Table S1 revealed that the interlayer spacing of MnO_2 decreased from 7.29 Å (pristine MnO_2) to 7.24 Å for Ni-MnO_2, 7.25 Å for Co–MnO_2, 7.18 Å for Cu–MnO_2 and 7.28 Å for Zn–MnO_2. The fast diffusion and substitution of K^+ by M^{2+} benefited from the unique

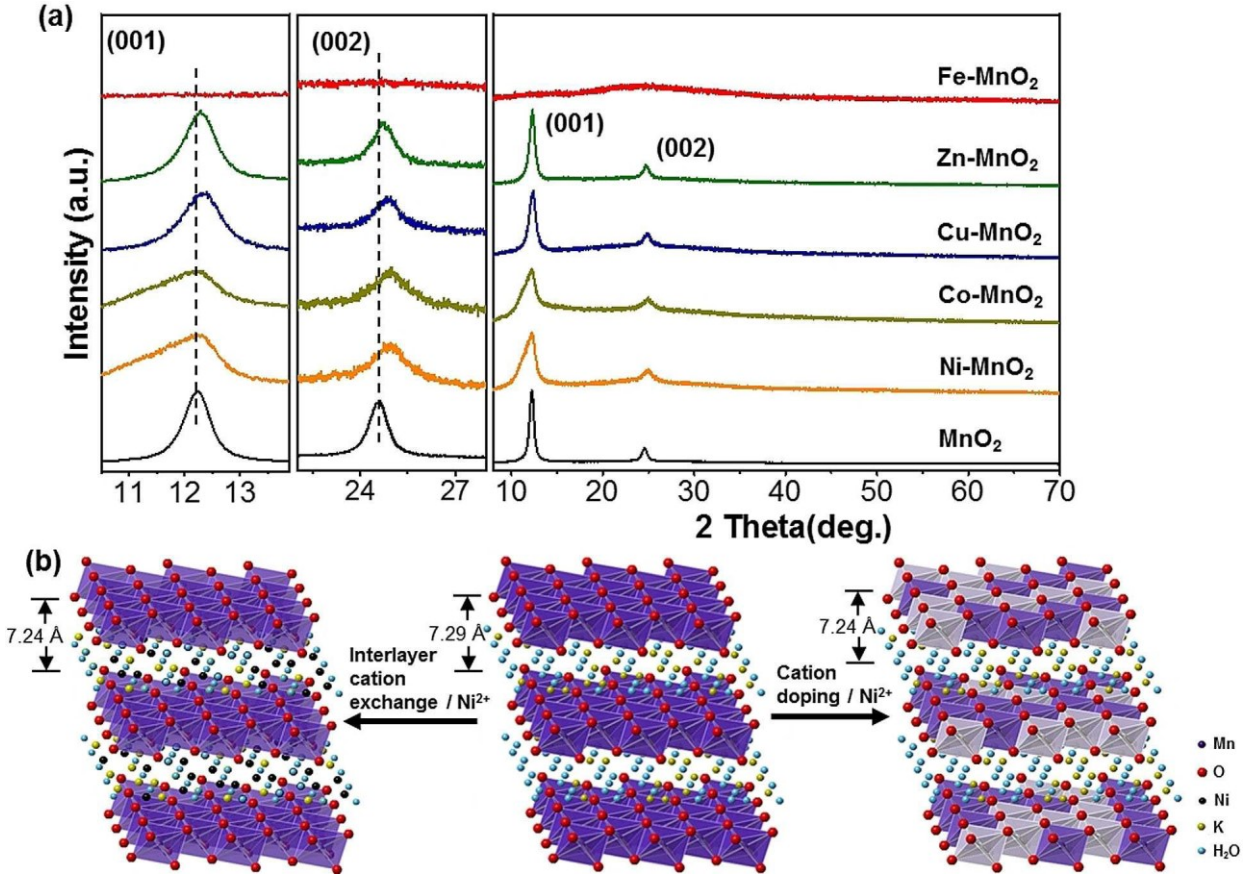

Figure 2. (a) XRD spectra and enlarged (001) and (002) Brag reflection for pristine MnO_2 and intercalated Ni–MnO_2, Co–MnO_2, Cu–MnO_2, Zn–$MnO_2$and Fe–MnO_2nanosheets via cation exchange. (b) Schematic illustration of the interlayer intercalation and lattice doping of layered MnO_2 nanosheets with Ni^{2+} cation.

layered structure and is illustrated in Figure 2b, demonstrating the visible change of the interlayer spacing. Since the interlayer spacing is sensitive to the guest species, less steric hindrance and enhanced electrostatic attraction are responsible for the shrinkage and contraction of the interlayer spacing after the replacement of K^+ (radius = 1.38 Å) with smaller divalent cations Ni^{2+} (0.69 Å), Co^{2+} (0.74 Å), Cu^{2+} (0.73 Å), and Zn^{2+}
(0.74 Å). As for Fe–MnO_2, a high concentration of Fe (71.4 at%) resulted in the disruption of layered nanosheets; while smaller disks were seen in Figure 1h, similar to previous results from Teng *et al.*[5] This morphology transformation was also clear from the XRD diffraction (Figure 2a). The amorphous materials were obtained after exchanging with Fe^{3+}. This was mainly attributed to the disruption of the crystal structure of MnO_2 caused by the heavily doped Fe in the crystal lattice as well as the intercalated high-valence cation residing in the interlayer region.

Electrocatalysis

The electrocatalytic OER activity of pristine MnO_2 and M–MnO_2 nanosheets was examined by linear scan voltammetry (LSV) in O_2-saturated 1 M KOH using a standard three-electrode configuration. As shown in Figure 3a, Ni-MnO_2 nanosheets were quite active with a considerably low overpotential ($\eta = 330$ mV) at a current density of 10 mA cm^{-2}, which was significantly lower than that of pristine MnO_2 nanosheets ($\eta = 581$ mV). Amorphous Fe-MnO_2 and low crystalline Co–MnO_2 showed moderate activity towards OER with relatively low overpotentials at 410 and 448 mV, respectively. In contrast, larger overpotentials of 485 and 508 mV were required to attain a current density of 10 mA cm^{-2} for Cu and Zn intercalated MnO_2 nanosheets, approximately 100 mV lower than that of MnO_2 nanosheets (Figure 3c). The improved OER activity induced by interlayer cation exchange was also suggested by the turnover frequencies (TOF) calculated from LSV measurements at $\eta = 450$ mV (Table 3). The highest TOF of 0.0356 s^{-1} was obtained with Ni-MnO_2, followed by Fe–MnO_2 (0.0163 s^{-1}) and Co–MnO_2 (0.0116 s^{-1}), which was significantly higher than that of pristine MnO_2 (0.0061 s^{-1}). Moreover, the accompanying Tafel plots further emphasized the superior and fast catalytic kinetics of intercalated MnO_2 nanosheets (Figure 3b). Specifically, the Tafel slope associated with Ni–MnO_2, Fe–MnO_2, and Co–MnO_2 were all around 22–25 mV dec^{-1}, much lower than that of pristine

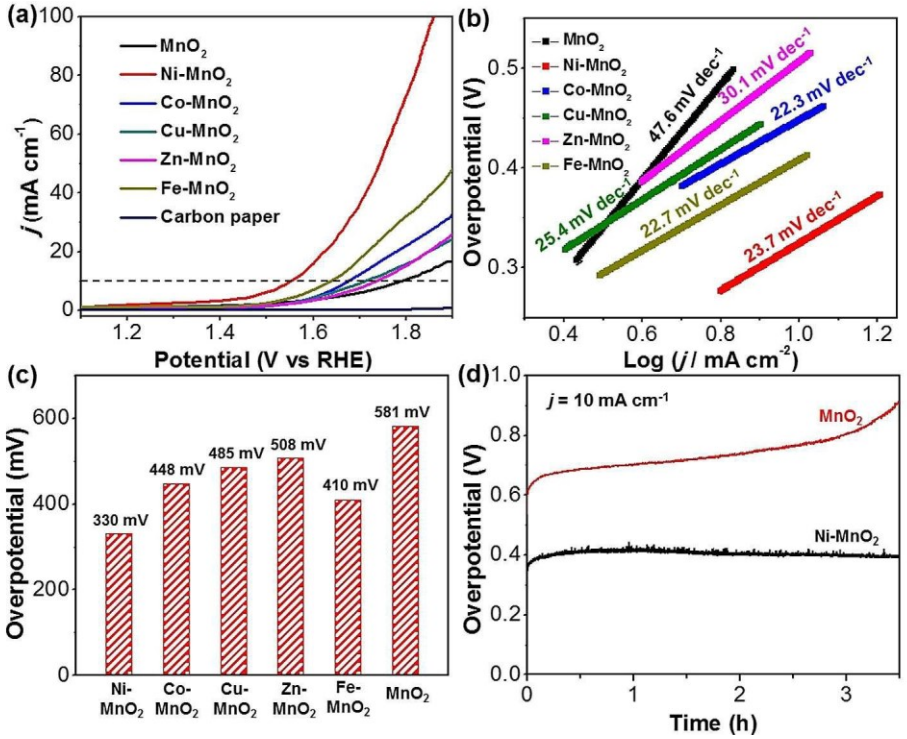

Figure 3. (a) Linear sweep voltammetry (LSV) curves of OER for pristine MnO_2, Ni–MnO_2, Co–MnO_2, Cu–MnO_2, Zn-MnO_2, and Fe–MnO_2 nanosheets in O_2-saturated 1 M KOH at a scan rate of 10 mV s^{-1}. (b) The corresponding Tafel plots for OER. (c) Comparison of overpotentials to reach 10 mA cm^{-2} for MnO_2, Ni–, Co–, Cu–, Zn–, and Fe–MnO_2 nanosheets via cation exchange. (d) Galvanostatic long-term durability test for the as-prepared nanocatalysts at a constant current density of 10 mA cm^{-2}.

MnO_2 nanosheets (47.6 mV dec^{-1}), suggesting a lower kinetic barrier for OER after intercalation.

The durability of as-prepared catalysts was evaluated by chronopotentiometry where the current density was maintained at 10 mA cm^{-2} (Figure 3d). In the case of pure MnO_2 nanosheets, the overpotential increased up to approximately 915 mV in 3.5 h to achieve the target current density at 10 mA cm^{-2}. This is consistent with the reported poor stability [6c,h,6g] of δ-MnO_2 in water oxidation. Whereas, an evident enhancement in stability occurred after Ni^{2+} intercalation where the nearly constant applied potential was performed over 3.5 h.

The overpotential was maintained at around 390–400 mV even with a slight decrease to obtain 10 mA cm^{-2} after 3.5 h electrolysis.

On the basis of those findings, the intercalation of metal cations in the interlayer regions of layered MnO_2 nanosheets is mainly responsible for the improvement of the catalytic activity for OER and stability. The changes in physiochemical properties of intercalated MnO_2 nanosheets, in terms of the average oxidation state of Mn, interlayer distance, electron transfer, and cooperative effects of metal cations/lattice Mn, will be discussed in detail to correlate the structure-function relationship. The activity of Fe–MnO_2 will not be further discussed below due to the morphological transformation and the disruption of the crystallinity of MnO_2.

Discussion

Average Oxidation State

Generally, the OER catalyzed by metal oxide in alkaline media undergoes five elementary steps [Eq. (1)–(5)] as below, where the reaction in Equation (3) is the rate-determining step:

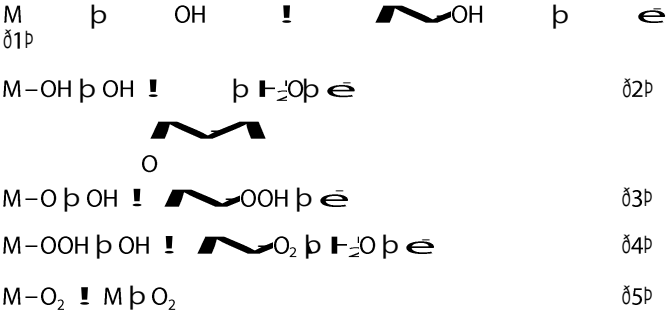

The Mn^{3+}-rich structured manganese oxides are proven to be more active than other MnO_x, since the unstable Mn $^{3+}$ sites in the MnO_6 octahedra are prone to adsorb the OH^- species and form MnOOH intermediates, kinetically accelerating the oxygen evolution.[9a,26] Smith *et al.* showed that Mn^{3+} enriched Mn_2O_3 and γ-MnOOH stood out for water oxidation catalysis by comparing various crystalline oxides consisting of Mn^{3+}, Mn^{4+}, and mixed-valence manganese oxides.[10a] Additionally, the insertion of Ca or Ag into the tunnel sites of α-MnO_2 (OMS-2) leading to the substantial increase of Mn^{3+} fraction was

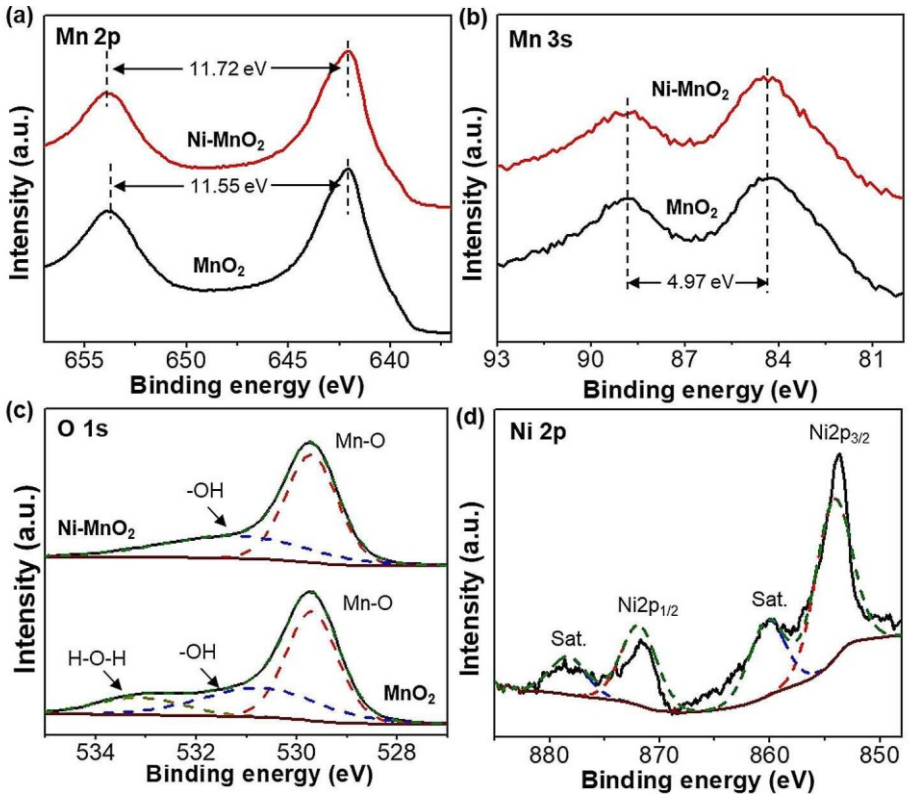

Figure 4. XPS analysis of the pristine MnO_2 and Ni–MnO_2nanosheets. High resolution (a) Mn 2p (b) Mn 3 s (c) O 1s spectra for MnO_2 and Ni–MnO_2 respectively. (d) High resolution Ni 2p spectra for Ni-MnO_2

Table 2. The summation of the surface elemental compositions obtained from the deconvoluted high resolution Mn 2p, Mn 3 s, and O 1s XPS spectra of the intercalated MnO_2 samples.

Sample	Mn $2p_{3/2}$ peak position [eV]	ΔE Mn 2p [eV]	ΔE Mn 3 s [eV]	$O_{lattice}$ (529.7 eV)	$O_{hydroxyl}$ (530.9 eV)	AOS (titration)
MnO_2	642.1	11.56	4.97	53.3	32.5	3.85 ± 0.04
Ni–MnO_2	642.2	11.64	4.97	63.4	36.6	3.81 ± 0.04
Co–MnO_2	642.2	11.61	4.98	66.8	33.2	3.85 ± 0.05
Cu–MnO_2	642.3	11.57	4.98	63.9	36.1	3.82 ± 0.03
Zn–MnO_2	642.3	11.68	4.32[a]	67.6	34.2	3.84 ± 0.02

[a] ΔE Mn 3 s = 4.32 eV of Zn–MnO_2 due to the overlapping with Zn 3p.

reported by Li *et al.*[11b] Lucht *et al.* stated that the layer Mn^{4+} of birnessite would convert to Mn^{3+} as the cations (*i.e.,* Be, Mg, Zn, B, Al, and Ga) intercalated into the interlayer region.

To uncover the change in surface Mn valence or average oxidation state (AOS) of our intercalated MnO_2 nanosheets, X-ray photoelectron spectroscopy (XPS) spectra were collected (Figures 4 and S3). The relative positions of the Mn $2p_{3/2}$ and the magnitude of the 2p, 3s multiplet splitting (ΔE 2p and ΔE 3s) extracted from the experimental spectra are summarized in Figures 4a, b and Table 2. For pristine MnO_2, the Mn $2p_{3/2}$ peak binding energy (BE) of 642.1 eV with a spin energy separation between the Mn $2p_{1/2}$ and Mn $2p_{3/2}$ of 11.56 eV (ΔE 2p) agrees with the literature value for Mn^{4+} (Figure 4a, Table 2).[27] In Ni-MnO_2, the ΔE 2p increased to 11.64 eV, indicating a slight increase of lower oxidation states, *e.g.,* Mn^{2+} and Mn^{3+}, after intercalation. Nevertheless, there was nearly no change in the multiplet splitting of Mn 3s peak for MnO_2 and Ni-MnO_2 (~ 4.97 eV, as shown in Figure 4b). This may be ascribed to the surface concentration of Mn species with lower oxidation states being very low. Similar results were also observed for Co–MnO_2 (Figure S4). Moreover, the exchanged metal cations in the intercalated MnO_2 nanosheets were mainly in divalent states (Figure S5). As given in Figure 4d, for Ni–MnO_2, two pronounced peaks at 853.9 and 872.0 eV with two shake-up satellites are characteristic for Ni^{2+} in the Ni 2p region.[28] All of the other intercalated metal cations displayed the divalent state, suggesting successful cation exchange without any redox behavior.

The AOS of MnO_2 nanosheets were further measured using a thiosulfate titration method.[13] Since the titration measures the oxidation states of Mn after digesting the MnO_2 nanosheets, the AOS values represent the average Mn valence of the bulk. Those results are summarized in Table 1, which gives direct

Table 3. Summary of OER activity, electrochemical active surface area and electrochemical impedance for MnO_2, Ni–MnO_2, Co–MnO_2, Cu–MnO_2, Zn–MnO_2 and Fe–MnO_2 catalysts.

Sample	TOF (at $\eta = 0.45$ V) [s^{-1}]	Double layer capacity C_{dl} [mF cm^{-2}]	EIS R_{ct} [Ω]	k^0 [$\times 10^{-8}$ cm s^{-1}]
MnO_2	0.0061	6.1	3325	4.1
Ni–MnO_2	0.0356	15.8	52.0	262.1
Co–MnO_2	0.0116	33.9	67.1	203.1
Cu–MnO_2	0.0091	17.6	3629	3.8
Zn–MnO_2	0.0074	15.2	3717	3.7

evidence for the decrease in the AOS of all M–MnO_2. For example, Ni–MnO_2 exhibits the lowest oxidation state of Mn, 3.81 ± 0.04; while pristine MnO_2 nanosheets have an AOS of 3.85 ± 0.04. The change in the AOS of Mn is very small (0.04), which also does not follow any trend with OER activity of intercalated MnO_2 nanosheets. Therefore, changes in activity are not solely explained by the change in oxidation state of Mn. More characterization of electrochemical properties and vibrational spectra were conducted to explore multiple factors affecting the OER activity and stability.

In addition, the change in the surface O species was measured in the O 1s region (Figure 4c). For pristine MnO_2, three distinguishable deconvolution peaks at 529.7, 530.9 and 533.1 eV were attributed to lattice oxygen (O^{2-}), hydroxyl groups (–OH), and adsorbed water molecules, respectively. While in the case of Ni-MnO_2, the proportion of O^{2-} increased from 53.3% for MnO_2 to 63.4% and the adsorption of molecular water became negligible (similarly observed for Co–, Cu–, Zn–MnO_2 in Table 2). These results suggest that the decreased interlayer spacing is unfavorable for the accommodation and fluctuation of water molecules, known as a key factor to tune the activity of the OER.[14]

Interlayer Spacing, Electrochemical Surface Area (ECSA) and Charge Transfer

To prove the interlayer-associated OER activity, the electrochemically active surface area (ECSA) of prepared catalysts was determined by double layer capacity measurements from 1.07 to 1.17 V vs. RHE in 1 M KOH (Figure S6). Table 3 summarized the obtained double layer capacity (C_{dl}) for all the catalysts and the C_{dl} is linearly proportional to ECSA. As depicted in Figure 5a, the relative enhancement was observed in the intercalated MnO_2 compared to pristine MnO_2 (6.1 mF cm^{-2}), but the most active Ni-MnO_2 possessed a moderate surface area of 15.8 mF cm^{-2} and Co–MnO_2 even showed the highest surface area of 33.9 mF cm^{-2} among all the catalysts. This result suggests that the improvement of the OER activity is unlikely related to exposed surface area; instead, the OER should occur in the interlayer regions where the intercalated cations reside.

Furthermore, the electrochemical impedance spectroscopy (EIS) studies were conducted at an overpotential of 0.47 V in 1 M KOH to evaluate the catalytic kinetics of the prepared materials. The equivalent circuit curves fit very well with the Nyquist plots in Figure 5b and the charge transfer resistance (R_{ct}) and the rate constant (k^0) are listed in Table 3. Not surprisingly, the Ni–MnO_2 exhibited the lowest transport impedance and the charge transfer resistance of 52.0 Ω, followed by Co–MnO_2 (67.1 Ω). In contrast, the R_{ct} values of Cu–MnO_2 and Zn–MnO_2 are two orders of magnitude larger, close to that of pristine MnO_2 (3325 Ω). These fitting results indicate the accelerated charge transfer and fast catalytic kinetics between layers are ascribed to the reduced steric hindrance and decreased interlayer distance after Ni and Co intercalation. Hence, the modification of interlayer environments mainly contributes to the improved OER activity, consistent with the literature.[14,29]

Vibrational Characterization

How the intercalated cations affect the interlayer environment or the cooperative effect across the interlayer of MnO_2 is still ambiguous. Vibrational spectroscopic technologies including Fourier-transform infrared spectroscopy (FTIR) and Raman spectroscopic are particularly attractive, due to their high sensitivity to the local structures of manganese oxide materials. FTIR and Raman spectroscopy can offer more comprehensive and reliable evaluation of structural properties. The similarity in

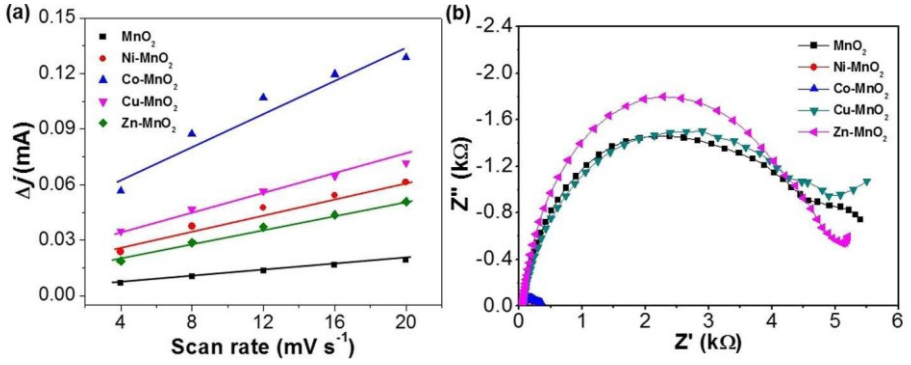

Figure 5. (a) The capacitive current densities at 1.12 V vs RHE as a function of scan rate for MnO_2, Ni–MnO_2, Co–MnO_2, Cu–MnO_2, Zn-MnO_2 and Fe–MnO_2 in 1 M KOH solution. (b) Nyquist plots of the prepared materials at an overpotential of 0.47 V.

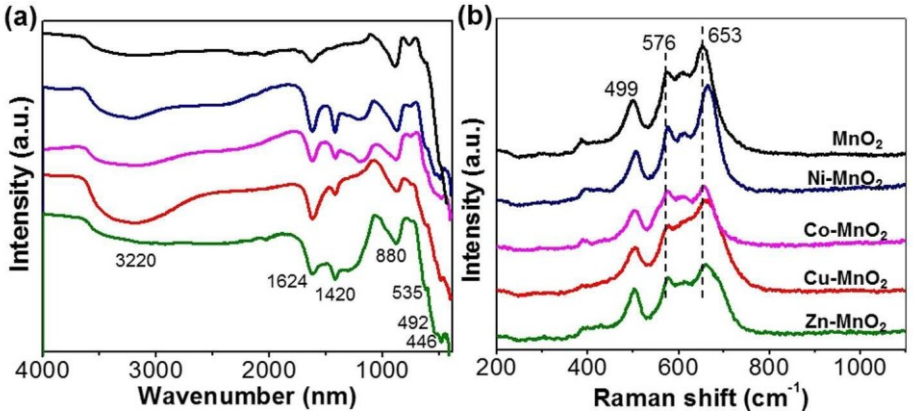

Figure 6. (a) FT-IR spectra and (b) Raman spectra of the pristine MnO_2, Ni–MnO_2, Co–MnO_2, Cu–MnO_2, Zn–MnO_2, and Fe–MnO_2 nanosheets.

FTIR spectra gave supportive evidence for retaining of the crystal structure of MnO_2 nanosheets for all samples. Especially in the range of lower wavenumbers (<700 cm^{-1}), characteristic bands at 535, 492 and 446 cm^{-1} are assigned to Mn–O stretching modes in MnO_6 octahedra layers in MnO_2 (Figure 6a).[30] The broad band at around 3220 cm^{-1} and peaks located at 1624 and 1420 cm^{-1} are attributed to the symmetric stretching vibrations and O–H bending vibration of hydroxyl groups, respectively.[31]

More detailed vibrational spectroscopic data were further collected by using Raman spectroscopy (Figure 6b). For pristine MnO_2, the two pronounced high-wavenumber bands along with two rather low intense bands <500 cm^{-1} are consistent with the reports for δ-MnO_2.[32] As determined from Raman simulations, Raman-active modes with $3A_g + 6\ B_g$ species are usually shown in MnO_2 materials (*i.e.,* birnessite structured δ-MnO_2) with monoclinic C2/m space group. Accordingly, the most prominent Raman bands for pristine MnO_2 at 653 cm^{-1} were due to the out-of-plane v_1(Mn–O) symmetric stretching vibrations along the interlayer direction in the MnO_2 framework, which is assigned to A_{1g} symmetric mode in the C_{2h}^3 spectroscopic space group.[33] The band at 576 cm^{-1} is a specific fingerprint of in-plane stretching vibrations v_2(Mn–O) of MnO_6 groups along the layer chains. Intercalated M–MnO_2 all preserved the inherent spectral features of the δ-MnO_2 nanosheets with distinguishable v_1 and v_2 modes. The weakening and broadening of the v_1 and v_2 modes revealed an increased degree of structural disorder for M–MnO_2, which is ascribed to a strong Jahn-Teller effect induced by the intercalation of cations in the interlayer region.[34] This is in good agreement with the XRD results (Figure 2a). An obvious blue shift of the v_1 stretching frequency to higher wavenumber 664 cm^{-1} was observed after Ni intercalation, indicative of the strengthening of the Mn–O bonds perpendicularly to the layer chains. The elongation of the MnO_6 octahedra along the interlayer direction is attributed to the enhanced interaction between the basal Mn and intercalated metal cations. The incorporation of metal cations into the interlayer spacing caused local lattice distortion where the increase of the v_1 vibrational mode occurred. In addition, the increased intensity ratio of v_2/v_1 vibrational modes implied enhanced polarizability, which directly resulted from the replacement of K^+ with more positive transition metal cations.[35] Thus, the readily intercalated transition metal cations result in the enhancement of the OER activity by varying the interlayer environment and interactions between layers.

Comparison Between In-Plane Doping and Interlayer Intercalation

The interlayer-associated OER activity enhancement was further confirmed by control experiments of the in-plane doping of Ni into MnO_2 nanosheets. The in-plane Ni-doped MnO_2 was obtained by synthesizing MnO_2 in the presence of $Ni(NO_3)_2$, denoted as Ni-doped MnO_2. As shown in Figure 7a, the XRD diffraction peaks corresponding to (001) and (002) planes of Ni-doped MnO_2 also shifted to higher values with peak broadening, similar to the intercalated Ni–MnO_2. The reductions in the interlayer distance and crystallinity were ascribed to the substitution of Mn by Ni in the planes.[33] The Raman vibrations of Ni-doped MnO_2 resembled that of Ni–MnO_2, where a 12 cm^{-1} shift to high-wavenumber for v_1 mode was also observed (Figure 7b). This shift to a higher vibration frequency, again, indicated the strengthening of the Mn–O bonds along the interlayer direction in the Ni-doped MnO_2. Therefore, the effective partial replacement of Mn by smaller Ni mainly accounts for the stronger network energy of the Ni-doped materials. As a control, we used excessive K^+ to exchange or extract the doped Ni ions. Consequently, no discernible changes in XRD and Raman spectra were found for Ni-doped MnO_2/K^+ (K^+ intercalation after in-plane Ni-doping), showing the difficulty in replacing Ni embedded in the in-plane layers via simple ion exchange.

Considering similar trends of varying properties, we compared the electrocatalytic activity of Ni-doped MnO_2 and Ni-MnO_2 nanosheets as shown in Figure 8. The overpotential at 10 mA cm^{-2} is 426 mV, 155 mV lower as compared to pristine MnO_2. This demonstrates the enhancement in OER activity

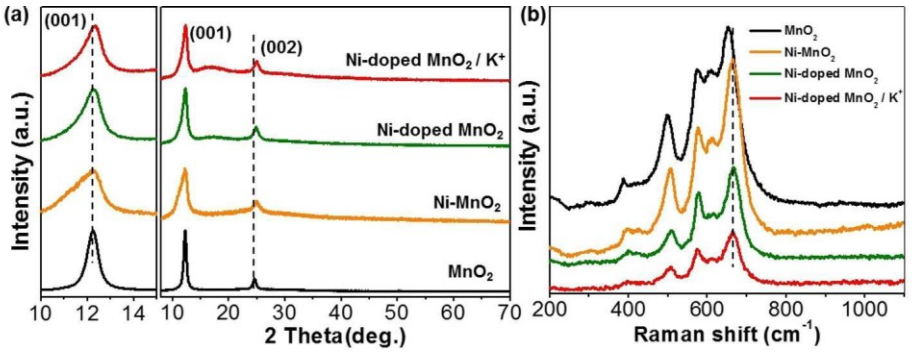

Figure 7. (a) XRD patterns and (b) Raman spectra for MnO_2, Ni–MnO_2, Ni-doped MnO_2, and Ni-doped MnO_2/K^+ respectively.

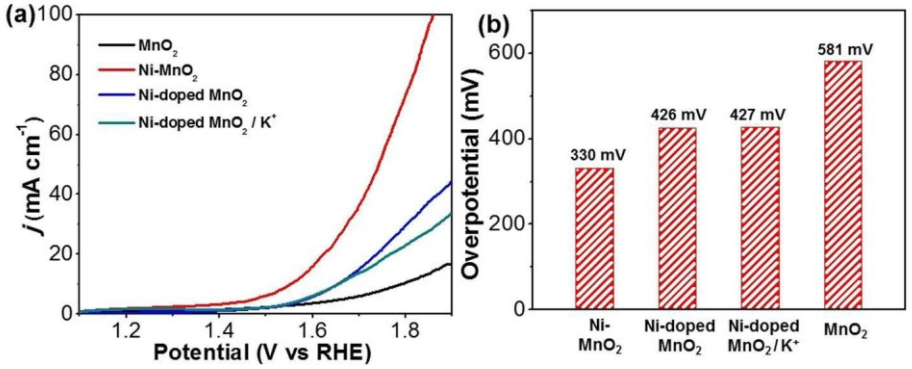

Figure 8. (a) Linear sweep voltammetry (LSV) curves of OER for pristine MnO_2, Ni–MnO_2, Ni-doped MnO_2, and Ni-doped MnO_2/K^+ nanosheets in O_2-saturated 1 M KOH at a scan rate of 10 mV s^{-1}. (b) Comparison of overpotentials to reach 10 mA cm^{-2} for MnO_2, Ni-doped MnO_2 and Ni-doped MnO_2/K^+ nanosheets.

resulting from cooperative effects between Mn and neighbor doped Ni.[37] Ni-doped MnO_2 is still less active than that of Ni-MnO_2 ($\eta = 330$ mV at 10 mA cm^{-2}).

The difference in the OER activity of intercalated and in-plane doped MnO_2 nanosheets clearly shows that the mobility of Ni ions is critical to the different interlayer environments. As verified by the afore-mentioned results, the OER catalysis is prone to occur in the interlayer regions where mobile cations serve as the active sites. The modifications and interactions between the layers are essential to the OER catalysis. Based on our experimental findings, the intercalated Ni^{2+} ions likely influence the cooperative binding of water or oxo during O_2 generation. In small-molecule Mn complexes, the formation of $Mn^{3+/4+}$–(μ-O)–$Mn^{3+/4+}$ is often observed as a key intermediate for catalytic O–O bond formation.[38] Hence, the function of Ni incorporation can be twofold, i) distorting the di-μ-oxo bridge between Mn and a fraction of weak metal-oxo bridges formed instead of easily eliminating O_2; and ii) dynamically moving between layers to allow a change in Mn distances between the two layers.[39] The interlayer cooperative effect accordingly facilitates the elongation or breaking of the Mn–O bond, eventually promoting O_2 generation. In the case of Ni-doped MnO_2 where substituted Ni^{2+} ions were trapped in the lattice, a local distortion of MnO_6 octahedra was also observed. The restricted local Mn–O species have limited reactivity due to the lack of mobility of Ni^{2+}. More dynamic interlayer sites with intercalated Ni^{2+} ions are of great importance in reducing the energy barrier of O–O bond formation.[40] In addition, the cooperative effect between Mn and the intercalated cations (Ni^{2+} ions) that are known to form di-μ-oxo bridges themselves,[41] cannot be ruled out with our current results, since other cations (Co^{2+} and Zn^{2+}) do not significantly promote oxygen evolution.

Conclusions

In summary, we investigated the effect of intercalated transition metal cations into the interlayer region of octahedral layered (OL-1) MnO_2 nanosheets, including Ni^{2+}, Co^{2+}, Cu^{2+}, Zn^{2+}, and Fe^{3+} ions. The intercalation of Ni^{2+} ions showed a remarkable enhancement of OER activity and long-term stability with the lowest overpotential of 330 mV to achieve the current density of 10 mA cm^{-2} and highest TOF of 0.0356 s^{-1} in comparison to pristine MnO_2 nanosheets ($\eta = 581$ mV, TOF = 0.0061 s^{-1}) and among other intercalated MnO nanosheets. Detailed structural analysis and electrochemical characterization were used to study the likely mechanisms that contributed to the improvement of OER activity. The modification of interlayer environments mainly contributes to the improved OER activity

other than changes on the surface of MnO_2 nanosheets. Ni intercalation, different from other metal cations, strengthens the Mn–O bond perpendicular to the layer chains to further facilitate the interlayer catalysis possibly between two Mn sites. Compared to the trapped Ni^{2+} ions in the case of Ni-doped MnO_2, more dynamic Ni^{2+} ions intercalated between layers are benefical to O–O bond formation across the entire layer, thus promoting the OER. The demonstrated intercalation effect highlights a facile and effcient strategy applicable to other layered materials and provides new opportunities to develop highly efficient OER catalysts.

Experimental Section

Materials: Potassium permanganate ($KMnO_4$, ≥99.0%), sodium dodecyl sulfate (SDS, ≥99.0%), concentrated sulfuric acid (H_2SO_4, 95.0–98.0%), cobalt(II) nitrate hexahydrate ($Co(NO_3)_2{\cdot}6H_2O$, ≥98%), copper(II) nitrate trihydrate ($Cu(NO_3)_2{\cdot}3H_2O$, 99–104%), nickel(II) nitrate trihydrate ($Ni(NO_3)_2{\cdot}6H_2O$, 98%), iron(III) nitrate nonahydrate ($Fe(NO_3)_3{\cdot}9H_2O$, ≥98%), zinc(II) nitrate hexahydrate ($Zn(NO_3)_2{\cdot}6H_2O$, 98%), ethanol, Vulcan XC 72R carbon black, Nafion perfluorinated resin solution (5 wt% in lower aliphatic alcohols and water, contains 15–20% water) were purchased from Sigma-Aldrich and used as received. Deionized water (High-Q, Inc. 103 S Stills) with a resistivity of >10.0 MΩ was used throughout the experiments.

Synthesis of MnO_2 nanosheets: MnO_2 nanosheets were synthesized using a previously reported procedure.[19] 0.92 g (3.2 mol) of SDS was first dissolved in 315 mL distilled water containing 1.6 mL of 0.1 M H_2SO_4. The mixture was refluxed for 10 min. Then, 3.2 mL of 50 mM $KMnO_4$ (25.3 mg) aqueous solution was added to the above solution under vigorous stirring. The reaction was further refluxed for 1 h. The MnO_2 nanosheets were collected by centrifugation and washed with distilled water for three times. The purified MnO_2 nanosheets were redispersed and stored in water (1 mg mL^{-1}) for further characterization and synthesis.

Synthesis of intercalated M–MnO_2 (M=Ni, Co, Cu, Zn, Fe) nanosheets: Cation intercalated MnO_2 (denoted as M–MnO_2, M=Ni, Co, Cu, Zn, Fe) nanosheets were synthesized by a simple cation exchange method. 10 mL of the as-prepared MnO_2 nanosheets colloidal solution (1 mg mL^{-1}) was diluted in 90 mL distilled water. The solution with multivalent cationic nitrate salts (the molar ratio of M:Mn = 3:1) was added and the suspended MnO_2 flocculated immediately. The mixture was stirred for overnight at room temperature, collected by centrifugation and washed with water for three times to remove the free nitrate salts. The purified M–MnO_2 was redispersed in water for further electrochemical characterization.

Synthesis of Ni-doped MnO_2 nanosheets: Ni-doped MnO_2 nanosheets were synthesized similar to the procedure of pristine MnO_2 nanosheets except the introduction of the Ni salt. 315 mL of aqueous solution containing 0.92 g (3.2 mol) SDS and 1.6 mL of H_2SO_4 (0.1 M) was refluxed for 10 min. Then, 3.2 mL of 50 mM $KMnO_4$ and 5 mM $Ni(NO_3)_2{\cdot}6H_2O$ (the molar ratio of Ni:Mn = 0.1:1) was rapidly added under vigorous stirring. The reaction was further refluxed for 1 h. The obtained suspension was centrifuged and washed with distilled water for three times, then redispersed in water (1 mg mL^{-1}) and kept for further characterization.

Titration by thiosulfate to determine the average oxidation state (AOS) of Mn: The AOS of Mn in each intercalated sample was determined by titration with sodium thiosulfate.[13] Typically, 10 mg of various nanosheets were first dissolved in 1 mL of NaOH/NaI solution (3.2 g of NaOH, 6 g of NaI, and 10 mL of water) and 2 mL of 20 vol% sulfuric acid solution. After the complete dissolution of the powder, the red solution was titrated with 5 mM sodium thiosulfate solution until the color turned to pale yellow. After adding 4 mL of starch indicator solution (2 mg mL^{-1}), more thiosulfate solution was dropped until the blue color disappeared and the solution became colorless. The consumed volume of thiosulfate was recorded to determine the AOS of Mn [Eq. (6)]:

$$AOS = 2 \times [1 + 0.5 \times n(Ox)/n(Mn)] \quad (6)$$

where, n(Ox) is the mole of oxidized equivalents (thiosulfate), n(Mn) is the mole of Mn. Three measurements were carried out for each sample to calculate the standard derivation.

Characterizations: Transmission electron microscopy (TEM) was performed with a FEI Tecnai 12 G2 Spirit Bio TWIN with an accelerating voltage of 120 kV. TEM samples were prepared by casting the suspension of materials on a carbon coated copper grid (400 mesh). Scanning electron microscopy (SEM) was carried out using a FEI Nova NanoSEM 450, equipped with energy dispersive X-ray spectroscopy (EDX) microanalysis. An accelerating voltage of 10 kV and a beam current of 10 mA was applied. SEM samples were prepared by casting a suspension of the materials on silicon wafers. The wide-angle X-ray diffraction (XRD) patterns over a 2θ range of 5–80° with a continuous scan rate of 0.25°/min were recorded using a Bruker D2 Phaser powder diffractometer (Cu Kα radiation, λ = 1.5406 Å) with an operating voltage of 40 kV and a current of 44 mA. The quantitative elemental compositions of samples were determined by X-ray fluorescence (XRF) with a Rigaku ZSX Primus IV sequential wavelength-dispersive XRF spectrometer (4 kW Rh anode). X-ray photoelectron spectroscopy (XPS) analysis of the synthesized materials was conducted on a PHI model Quantum 2000 spectrometer with scanning ESCA multiprobe (Physical Electronics Industries Inc.) using Al Kα radiation (λ = 1486.6 eV) as the radiation source. The spectra were recorded in the fixed analyzer transmission mode with pass energies of 187.85 eV and 29.35 eV for recording survey and high resolution spectra, respectively. Binding energies (BE) were measured for Cu 2p, Co 2p, Ni 2p, Fe 2p, Zn 2p, Mn 2p, Mn 3 s, and O 1s regions. The XPS spectra were analyzed and fitted using CasaXPS software (version 2.3.16). Sample charging effects were eliminated by correcting the observed spectra with the C 1s BE value of 284.8 eV. Atomic force microscopy (AFM) was conducted with a Nanosurf NaioAFM spectrometer under tapping mode at room temperature in air. AFM samples were prepared by casting on a graphite substrate. Raman spectra were obtained on a Renishaw 2000 Raman scope with 50× microscope objective and an Ar ion laser (514.4 nm) as the excitation source. Fourier-transform infrared spectroscopy (FTIR) was performed on a NICOLET MAGNA 560 FTIR spectrometer in transmission mode (32 scans, 4 cm^{-1} resolution). The surface area of as-synthesized materials was evaluated by the Brunauer–Emmett–Teller (BET) method on a Nova 2000e apparatus. The samples were degassed for 6 h before nitrogen adsorption measurements and the specific surface area was calculated using the BET equation.

Electrochemical measurements: All electrochemical measurements were performed using a standard three-electrode cell with a CHI 627E electrochemical potentiostat. The Ag/AgCl electrode (saturated with KCl, $E_{Ag/AgCl}$ = 0.197 V, at 25 °C) and platinum wire was employed as the reference electrode and counter electrode, respectively. A piece of carbon paper (1 cm × 1 cm) casted by catalyst ink was adopted as the working electrode. The aqueous dispersion of purified catalysts without drying (500 μL, 8 mg mL^{-1}) was directly mixed with 500 μL of Vulcan XC-72R carbon suspension (2 mg mL^{-1} in ethanol) by sonication avoiding the aggregation of nanosheets. Then 92 μL of 5 wt% Nafion solution was added and

sonicated for another 20 mins. About 50 μL of the catalyst ink was drop-casted on the carbon paper and dried overnight before use. All potentials presented in this work are calibrated to the reversible hydrogen electrode (RHE) using the Nernst equation: $E_{RHE} = E_{Ag/AgCl} + 0.059 \times pH + 0.197$. Linear sweep voltammetry (LSV) was *i*R-compensated and recorded at a scan rate of 10 mV s^{-1} over the range of 1.0 to 1.8 V (vs RHE) in O_2-saturated 1 M KOH solution. Non-faradaic double layer capacity measurements were conducted from 1.03 to 1.13 V in 1 M KOH with different sweeping rates between 4 and 20 mV s^{-1}. The electrochemical impedance spectra (EIS) were examined in the sweeping frequency from 100 to 0.01 kHz with an ac voltage of 5 mV amplitude. The applied potential was 1.7 V (vs RHE). The turnover frequency (TOF) value of OER is calculated with Equation (7) below:

$$TOF = (j \cdot A)/(4 \cdot F \cdot n) \quad (7)$$

where, j is the current density (mA cm^{-2}) obtained at $\eta = 0.45$ V from LSV measurements, A is the geometric area of the working electrode, F is the Faraday constant (96500 C mol^{-1}) and n is the number of moles of the catalyst.

Acknowledgments

J.H. thanks for the financial support from the University of Connecticut and National Science Foundation (CBET 1705566). Y.Y. acknowledges the support from the China Scholarship Council and Nanjing University of Science and Technology for her visiting at the University of Connecticut. SLS thanks the US Department of Energy, Office of Basic Energy Sciences, Division of Chemical, Biological and Geological Sciences under grant DE-FG02-86ER13622.A000 for support of this research. The SEM/TEM studies were performed in part at the Biosciences Electron Microscopy Facility of the University of Connecticut.

Conflict of Interest

The authors declare no conflict of interest.

Keywords: MnO_2 nanosheets · Cation intercalation · Interlayer environment · Oxygen evolution reaction

[1] a) M. W. Kanan, D. G. Nocera, *Science* **2008**, *321,* 1072–1075; b) S. Shafiee, E. Topal, *Energy Policy* **2009**, *37,* 181–189.
[2] a) A. Midilli, I. Dincer, *Int. J. Hydrogen Energy* **2008**, *33,* 4209–4222; b) Z. Zou, J. Ye, K. Sayama, H. Arakawa, *Nature* **2001**, *414,* 625; c) A. Kudo, Y. Miseki, *Chem. Soc. Rev.* **2009**, *38,* 253–278; d) H. Wang, H.-W. Lee, Y. Deng, Z. Lu, P.-C. Hsu, Y. Liu, D. Lin, Y. Cui, *Nat. Commun.* **2015**, *6,* 7261.
[3] D. R. MacFarlane, N. Tachikawa, M. Forsyth, J. M. Pringle, P. C. Howlett, G. D. Elliott, J. H. Davis, M. Watanabe, P. Simon, C. A. Angell, *Energy Environ. Sci.* **2014**, *7,* 232–250.
[4] a) R. Kötz, H. Lewerenz, S. Stucki, *J. Electrochem. Soc.* **1983**, *130,* 825–829; b) E. Antolini, *ACS Catal.* **2014**, *4,* 1426–1440.
[5] Y. Teng, X. D. Wang, J. F. Liao, W. G. Li, H. Y. Chen, Y. J. Dong, D. B. Kuang, *Adv. Funct. Mater.* **2018**, 1802463.
[6] a) Y. Umena, K. Kawakami, J.-R. Shen, N. Kamiya, *Nature* **2011**, *473,* 55; b) M. Huynh, C. Shi, S. J. Billinge, D. G. Nocera, *J. Am. Chem. Soc.* **2015**, *137,* 14887–14904; c) V. B. R. Boppana, S. Yusuf, G. S. Hutchings, F. Jiao, *Adv. Funct. Mater.* **2013**, *23,* 878–884; d) Y. Meng, W. Song, H. Huang, Z. Ren, S.-Y. Chen, S. L. Suib, *J. Am. Chem. Soc.* **2014**, *136,* 11452–11464; e) J. Yano, V. Yachandra, *Chem. Rev.* **2014**, *114,* 4175–4205.
[7] C.-H. Kuo, I. M. Mosa, S. Thanneeru, V. Sharma, L. Zhang, S. Biswas, M. Aindow, S. P. Alpay, J. F. Rusling, S. L. Suib, *Chem. Commun.* **2015**, *51,* 5951–5954.
[8] a) Y. Gorlin, T. F. Jaramillo, *J. Am. Chem. Soc.* **2010**, *132,* 13612–13614; b) D. M. Robinson, Y. B. Go, M. Greenblatt, G. C. Dismukes, *J. Am. Chem. Soc.* **2010**, *132,* 11467–11469.
[9] a) C.-H. Kuo, I. M. Mosa, A. S. Poyraz, S. Biswas, A. M. El-Sawy, W. Song, Z. Luo, S.-Y. Chen, J. F. Rusling, J. He, *ACS Catal.* **2015**, *5,* 1693–1699; b) A. Ramírez, P. Hillebrand, D. Stellmach, M. M. May, P. Bogdanoff, S. Fiechter, *J. Phys. Chem. C* **2014**, *118,* 14073–14081.
[10] a) P. F. Smith, B. J. Deibert, S. Kaushik, G. Gardner, S. Hwang, H. Wang, J. F. Al-Sharab, E. Garfunkel, L. Fabris, J. Li, *ACS Catal.* **2016**, *6,* 2089–2099; b) L. Mao, D. Zhang, T. Sotomura, K. Nakatsu, N. Koshiba, T. Ohsaka, *Electrochim. Acta* **2003**, *48,* 1015–1021.
[11] a) Z. Ye, T. Li, G. Ma, Y. Dong, X. Zhou, *Adv. Funct. Mater.* **2017**, *27,* 1704083; b) X. Li, J. Liu, Y. Zhao, H. Zhang, F. Du, C. Lin, T. Zhao, Y. Sun, *ChemCatChem* **2015**, *7,* 1848–1856.
[12] C. H. Kuo, W. Li, L. Pahalagedara, A. M. El-Sawy, D. Kriz, N. Genz, C. Guild, T. Ressler, S. L. Suib, J. He, *Angew. Chem. Int. Ed.* **2015**, *54,* 2345–2350; *Angew. Chem.* **2015**, *127*, 2375–2380.
[13] Y.-F. Shen, S. L. Suib, C.-L. O'Young, *J. Am. Chem. Soc.* **1994**, *116,* 11020–11029.
[14] Q. Kang, L. Vernisse, R. C. Remsing, A. C. Thenuwara, S. L. Shumlas, I. G. McKendry, M. L. Klein, E. Borguet, M. J. Zdilla, D. R. Strongin, *J. Am. Chem. Soc.* **2017**, *139,* 1863–1870.
[15] P. Xiong, R. Ma, N. Sakai, X. Bai, S. Li, T. Sasaki, *ACS Appl. Mater. Interfaces* **2017**, *9,* 6282–6291.
[16] a) A. C. Thenuwara, S. L. Shumlas, N. H. Attanayake, Y. V. Aulin, I. G. McKendry, Q. Qiao, Y. Zhu, E. Borguet, M. J. Zdilla, D. R. Strongin, *ACS Catal.* **2016**, *6,* 7739–7743; b) A. C. Thenuwara, E. B. Cerkez, S. L. Shumlas, N. H. Attanayake, I. G. McKendry, L. Frazer, E. Borguet, Q. Kang, R. C. Remsing, M. L. Klein, *Angew. Chem. Int. Ed.* **2016**, *55,* 10381–10385; *Angew. Chem.* **2016**, *128,* 10537–10541; c) A. C. Thenuwara, S. L. Shumlas, N. H. Attanayake, E. B. Cerkez, I. G. McKendry, L. Frazer, E. Borguet, Q. Kang, M. J. Zdilla, J. Sun, *Langmuir* **2015**, *31,* 12807–12813; d) I. G. McKendry, L. J. Mohamad, A. C. Thenuwara, T. Marshall, E. Borguet, D. R. Strongin, M. J. Zdilla, *ACS Energy Lett.* **2018**, *3,* 2280–2285; e) I. G. McKendry, A. C. Thenuwara, S. L. Shumlas, H. Peng, Y. V. Aulin, P. R. Chinnam, E. Borguet, D. R. Strongin, M. J. Zdilla, *Inorg. Chem.* **2018**, *57,* 557–564.
[17] a) Y. Sun, L. Wang, Y. Liu, Y. Ren, *Small* **2015**, *11,* 300–305; b) M. Pang, G. Long, S. Jiang, Y. Ji, W. Han, B. Wang, X. Liu, Y. Xi, *Electrochim. Acta* **2015**, *161,* 297–304; c) X. Zhang, P. Yu, H. Zhang, D. Zhang, X. Sun, Y. Ma, *Electrochim. Acta* **2013**, *89,* 523–529; d) S. Liu, Y. Zhu, J. Xie, Y. Huo, H. Y. Yang, T. Zhu, G. Cao, X. Zhao, S. Zhang, *Adv. Energy Mater.* **2014**, *4,* 1301960; e) B. Liu, I. M. Mosa, W. Song, H. Zheng, C.-H. Kuo, J. F. Rusling, S. L. Suib, J. He, *J. Mater. Chem. A* **2016**, *4,* 6447–6455.
[18] Y. Zhao, C. Chang, F. Teng, Y. Zhao, G. Chen, R. Shi, G. I. Waterhouse, W. Huang, T. Zhang, *Adv. Energy Mater.* **2017**, *7,* 1700005.
[19] Z. Liu, K. Xu, H. Sun, S. Yin, *Small* **2015**, *11,* 2182–2191.
[20] J. Huang, J. Chen, T. Yao, J. He, S. Jiang, Z. Sun, Q. Liu, W. Cheng, F. Hu, Y. Jiang, *Angew. Chem. Int. Ed.* **2015**, *54,* 8722–8727; *Angew. Chem.* **2015**, *127*, 8846–8851.
[21] W. Liu, H. Liu, L. Dang, H. Zhang, X. Wu, B. Yang, Z. Li, X. Zhang, L. Lei, S. Jin, *Adv. Funct. Mater.* **2017**, *27,* 1603904.
[22] a) Z. Ye, C. Qin, G. Ma, X. Peng, T. Li, D. Li, Z. Jin, *ACS Appl. Mater. Interfaces* **2018**, *10,* 39809–39818; b) F. Song, X. Hu, *J. Am. Chem. Soc.* **2014**, *136,* 16481–16484; c) H. Liu, Y. Wang, X. Lu, Y. Hu, G. Zhu, R. Chen, L. Ma, H. Zhu, Z. Tie, J. Liu, *Nano Energy* **2017**, *35,* 350–357.
[23] Y. Zhu, C. Cao, S. Tao, W. Chu, Z. Wu, Y. Li, *Sci. Rep.* **2014**, *4,* 5787.
[24] S. Devaraj, N. Munichandraiah, *J. Phys. Chem. C* **2008**, *112,* 4406–4417.
[25] N. H. Attanayake, A. C. Thenuwara, A. Patra, Y. V. Aulin, T. M. Tran, H. Chakraborty, E. Borguet, M. L. Klein, J. P. Perdew, D. R. Strongin, *ACS Energy Lett.* **2017**, *3,* 7–13.
[26] a) T. Takashima, K. Hashimoto, R. Nakamura, *J. Am. Chem. Soc.* **2012**, *134,* 1519–1527; b) D. M. Robinson, Y. B. Go, M. Mui, G. Gardner, Z. Zhang, D. Mastrogiovanni, E. Garfunkel, J. Li, M. Greenblatt, G. C. Dismukes, *J. Am. Chem. Soc.* **2013**, *135,* 3494–3501.
[27] H. Nesbitt, D. Banerjee, *Am. Mineral.* **1998**, *83,* 305–315.
[28] H. Yin, H. Tang, D. Wang, Y. Gao, Z. Tang, *ACS Nano* **2012**, *6,* 8288–8297.
[29] R. C. Remsing, I. G. McKendry, D. R. Strongin, M. L. Klein, M. J. Zdilla, *J. Phys. Chem. Lett.* **2015**, *6,* 4804–4808.
[30] B. J. Aronson, A. K. Kinser, S. Passerini, W. H. Smyrl, A. Stein, *Chem. Mater.* **1999**, *11,* 949–957.
[31] C. E. Frey, M. Wiechen, P. Kurz, *Dalton Trans.* **2014**, *43,* 4370–4379.

[32] C. Julien, M. Massot, R. Baddour-Hadjean, S. Franger, S. Bach, J. Pereira-Ramos, *Solid State Ionics* **2003**, *159*, 345–356.
[33] D. Rousseau, R. P. Bauman, S. Porto, *J. Raman Spectrosc.* **1981**, *10*, 253–290.
[34] K. P. Lucht, J. L. Mendoza-Cortes, *J. Phys. Chem. C* **2015**, *119*, 22838–22846.
[35] D. Chen, D. Ding, X. Li, G. H. Waller, X. Xiong, M. A. El-Sayed, M. Liu, *Chem. Mater.* **2015**, *27*, 6608–6619.
[36] a) A. Ogata, S. Komaba, R. Baddour-Hadjean, J.-P. Pereira-Ramos, N. Kumagai, *Electrochim. Acta* **2008**, *53*, 3084–3093; b) H. Yin, H. Li, Y. Wang, M. Ginder-Vogel, G. Qiu, X. Feng, L. Zheng, F. Liu, *Chem. Geol.* **2014**, *381*, 10–20.
[37] L. Ma, W. Zhang, P. Zhao, J. Liang, Y. Hu, G. Zhu, R. Chen, Z. Tie, J. Liu, Z. Jin, *J. Mater. Chem. A* **2018**, *6*, 20076–20082.
[38] a) M. Wiechen, H.-M. Berends, P. Kurz, *Dalton Trans.* **2012**, *41*, 21–31; b) K. J. Brewer, M. Calvin, R. S. Lumpkin, J. W. Otvos, L. O. Spreer, *Inorg. Chem.* **1989**, *28*, 4446–4451.
[39] I. Zaharieva, P. Chernev, M. Risch, K. Klingan, M. Kohlhoff, A. Fischer, H. Dau, *Energy Environ. Sci.* **2012**, *5*, 7081–7089.
[40] J. Yang, H. An, X. Zhou, C. Li, *J. Phys. Chem. C* **2015**, *119*, 18487–18494.
[41] K. Shiren, S. Ogo, S. Fujinami, H. Hayashi, M. Suzuki, A. Uehara, Y. Watanabe, Y. Moro-oka, *J. Am. Chem. Soc.* **2000**, *122*, 254–262.

Manuscript received: December 11, 2018
Revised manuscript received: January 8, 2019
Accepted manuscript online: January 29, 2019
Version of record online: February 27, 2019